Lagrangian transport by breaking surface waves

Luc Deike[1,2,3,†], **Nick Pizzo**[3] **and W. Kendall Melville**[3,†]

[1]Department of Mechanical and Aerospace Engineering, Princeton University, NJ 08540, USA

[2]Princeton Environmental Institute, Princeton University, NJ 08544, USA

[3]Scripps Institution of Oceanography, University of California San Diego, La Jolla, CA 92037, USA

The Lagrangian transport due to non-breaking and breaking focusing wave packets is examined. We present direct numerical simulations of the two-phase air–water Navier–Stokes equations describing focusing wave packets, investigating the Lagrangian drift by tracking tracer particles in the water before, during and after the breaking event. The net horizontal transport for non-breaking focusing packets is well described by the classical Stokes drift, both at the surface and in the bulk of the fluid, where the e-folding scale of the evanescent vertical profile is given by the characteristic wavenumber. For focusing wave packets that lead to breaking, we observe an added drift that can be ten times larger than the classical Stokes drift for a non-breaking packet at the surface, while the initial depth of the broken fluid scales with the wave height at breaking. We find that the breaking induced Lagrangian transport scales with the breaking strength. A simple scaling argument is proposed to describe this added drift and is found to be consistent with the direct numerical simulations. Applications to upper ocean processes are discussed.

Key words: air/sea interactions, ocean processes, wave breaking

---

1. Introduction

The object of this paper is to characterize the Lagrangian transport induced by breaking surface waves. It was shown by Stokes (1847) that linear surface waves possess, along with their harmonic orbital motion, a mean second-order drift or mass transport commonly referred to as Stokes drift. Waves in the ocean are not monochromatic and are rarely linear, and therefore a better description of this phenomenon under more realistic conditions is warranted for an improved understanding of upper ocean dynamics. Using direct numerical simulations, we investigate the Lagrangian transport due to wave breaking and propose a scaling model, finding that wave breaking leads to much greater transport than the traditional Stokes prediction.

The ocean and atmosphere interact strongly, controlling both weather and climate. This interaction occurs through the wavy surface separating the two. In particular, wave breaking modulates the transfer of mass, momentum and energy between the ocean and atmosphere (Melville 1996; Cavaleri, Fox-Kemper & Hemer 2012).

† Email addresses for correspondence: ldeike@princeton.edu, kmelville@ucsd.edu

However, wave breaking represents a two-phase unsteady turbulent flow, making theoretical, numerical and laboratory analyses difficult (Perlin, Choi & Tian 2013). Therefore, simple models based on physical arguments are valuable in serving as parameterizations in coupled ocean–atmosphere models.

The effect of Stokes drift on upper ocean dynamics, when averaging over scales much larger than those of the waves, enters through the so-called vortex force. That is, the vortex force is given by $u_s \times \omega$, where u_s is the Stokes drift and ω is the vorticity of the underlying flow. The vortex force is a consequence of the averaging and of Kelvin's circulation theorem, which for an inviscid fluid of uniform density has vortex lines moving with the fluid. Consequently, the Stokes drift provides a force to move surface vorticity due to surface boundary layers and wave breaking (Pizzo & Melville 2013), as well as passive tracers, to depth. Stokes drift has also been proposed as a mechanism for driving global ocean circulation (McWilliams & Restrepo 1999; Belcher *et al.* 2012) as well as providing a forcing term for Langmuir turbulence (Craik & Leibovich 1976; Sullivan & McWilliams 2010; D'Asaro 2014) and submesoscale ocean instabilities (Haney *et al.* 2015; McWilliams 2016).

Measurements of Stokes drift in the laboratory have often proved difficult. Longuet-Higgins (1953) showed the importance of viscosity in long-time mass transport. The description gets significantly more difficult when non-uniform waves are considered. Melville & Rapp (1988) used laser Doppler velocimetry, with relatively large measuring volumes that encompassed the surface displacement, to measure the velocity of particles at the surface in wave trains undergoing Benjamin–Feir instabilities that led to breaking. They found that the mean velocity of fluid at the surface, over very long-time averages, could be increased by a factor of up to two in the breaking region. Recently Grue & Kolaas (2017) experimentally investigated the Stokes drift associated with finite depth steep non-breaking propagating waves using particle tracking velocimetry and found that boundary layers enhance the surface drift. Note, Monismith *et al.* (2007) examined the drift due to very steep (and often breaking) waves and concluded that there was, pointwise, no mass transport in a case where both waves and shear current were present. Their study leaves large questions unanswered, such as where this vorticity in the interior of the fluid is coming from and how it interacts with the largely irrotational surface gravity waves.

Theoretical considerations of mass transport due to waves have progressed slowly since Stokes. Clamond (2007) extended the theory of Stokes for very steep Stokes waves, which was examined in the laboratory by Grue, Kolaas & Jensen (2014), Grue & Kolaas (2017). McIntyre (1981) highlighted the result from Longuet-Higgins & Stewart (1964) that showed the Eulerian return flow of a packet, due to gradients in its radiation stress, implies that there is no integral mass flux due to these packets. van den Bremer & Taylor (2016) discussed the effect of frequency dispersion and finite depth on the Stokes drift and the return flow. Furthermore, Eames, Belcher & Hunt (1994) showed the formal relationship between Stokes drift and Darwin drift (Darwin 1953), which is the permanent drift that occurs for particles in the path of a translating cylinder. These theories are limited to either narrow-banded or weakly nonlinear scenarios, and hence cannot describe the mass transport during breaking.

To elucidate the features of deep-water wave breaking, a dispersive focusing technique originally proposed by Longuet-Higgins (1974) has been successfully employed in the laboratory (Melville & Rapp 1985; Rapp & Melville 1990; Duncan, Qiao & Philomin 1999; Liu & Duncan 2003; Drazen, Melville & Lenain 2008; Tian, Perlin & Choi 2010; Perlin *et al.* 2013) and numerically (Dommermuth *et al.* 1988; Tian *et al.* 2010; Derakhti & Kirby 2014, 2016), together with compact breaking

waves simulations (Chen *et al.* 1999; Brucker *et al.* 2010; Iafrati 2011; Deike, Popinet & Melville 2015; Deike, Melville & Popinet 2016). This technique allows for 'black box' experiments, where one measures the (linear) properties of the surface wave field far upstream and downstream of the breaking event in order to deduce information about the (turbulent two-phase unsteady) breaking region. This has led to considerable progress in understanding the behaviour of the breaking-induced flow.

Based on laboratory experiments using this dispersive focusing technique, Drazen *et al.* (2008) proposed a scaling argument for the energy dissipation rate per unit length of breaking crest of the breaking-induced flow. This was corroborated using laboratory experiments and a breaking threshold parameter (Romero, Melville & Kleiss 2012), and was further confirmed by direct numerical simulations (Deike *et al.* 2015, 2016) and large eddy simulations (Derakhti & Kirby 2014, 2016). These studies showed that the relevant variables characterizing the post breaking flow are the acceleration due to gravity g and the height of the wave at breaking, h for both spilling and plunging breakers. Using similar arguments, Pizzo & Melville (2013) showed that the circulation of the breaking-induced mean flow could be scaled by these variables, as could the ratio of the energy in the breaking-induced mean flow to total energy lost (Pizzo, Deike & Melville 2016). Finally, Deike *et al.* (2016), Deike, Lenain & Melville (2017) showed that these quantities could be used to scale the air entrainment and the statistics of the bubble size distribution of the breaking-induced flow. Note that scalings of air entrainment and induced circulation by gravity and wave height were also discussed in Iafrati (2011).

Here we follow a similar strategy for the Lagrangian transport induced by breaking waves. We present direct numerical simulations of breaking waves created by the dispersive focusing technique described above. The accuracy of our numerical simulations has been previously demonstrated when investigating dissipation, current generation and air entrainment by breaking waves (Deike *et al.* 2015, 2016; Pizzo *et al.* 2016). The flow in the water is seeded by a large number of Lagrangian particles that are tracked during the breaking event. We compute the Lagrangian displacement of the particles and define the Lagrangian transport, or drift in the breaking region. The drift for breaking waves is found to depend on the breaking strength, that is the wave slope $S = hk$, with the height at breaking h and the characteristic wavenumber k, and can be up to ten times larger than the classical Stokes drift for a non-breaking focusing packet.

The paper is organized as follows, in § 2, we present the theoretical background for the Lagrangian transport by waves. A simple scaling argument that describes the added drift when a wave breaks is presented. In § 3, we describe the numerical methods and experiments used in this paper. In § 4, we describe the Lagrangian dynamics of non-breaking and breaking focusing wave packets. The vertical profile of the Lagrangian drift in the focusing and breaking area and the Lagrangian transport in the propagation direction, or added drift due to breaking, are discussed. We compare the numerical results with the linear theory presented earlier, as well as with the scaling argument, and reasonable agreement is found. We present conclusions and implications of this work in § 5.

2. Theoretical descriptions of Lagrangian transport by waves

The equation governing deep-water irrotational surface gravity waves is (see, for instance, § 3.1 of Phillips 1977)

$$\nabla^2 \phi = 0, \tag{2.1}$$

with boundary conditions

$$\eta_t + \phi_x \eta_x = \phi_z, \quad z = \eta, \tag{2.2}$$
$$\phi_t + \tfrac{1}{2}(\nabla\phi)^2 + g\eta = 0, \quad z = \eta, \tag{2.3}$$

and

$$\phi_z \to 0 \quad \text{as } z \to -\infty, \tag{2.4}$$

where ϕ is the velocity potential and η the free surface displacement. In this paper we consider two-dimensional waves, so that $\nabla = (\partial_x, \partial_z)$.

2.1. *Linear monochromatic waves: the classical Stokes drift*

For completeness, we begin by considering a deep-water monochromatic periodic surface gravity wave of constant amplitude a, with angular frequency ω and wavenumber given by the linear dispersion relationship $\omega^2 = gk$ where g is the acceleration due to gravity. To first order then,

$$\eta = a\cos(kx - \omega t); \quad \phi = \frac{a\omega}{k}\sin(kx - \omega t)e^{kz}. \tag{2.5a,b}$$

In the Lagrangian reference frame, we label a particle $x = (\xi, \zeta)$. The Eulerian and Lagrangian reference frames are then connected by

$$\frac{\mathrm{d}x}{\mathrm{d}t} = \nabla\phi|_{(x=\xi, z=\zeta)}. \tag{2.6}$$

Now, for a particle originally at $x_0 = (\xi_0, \zeta_0)$ this implies

$$\xi - \xi_0 = -a\sin(k\xi_0 - \omega t)e^{k\zeta_0}, \tag{2.7}$$
$$\zeta - \zeta_0 = a\cos(k\xi_0 - \omega t)e^{k\zeta_0}. \tag{2.8}$$

The Lagrangian velocity at a point is found by Taylor expanding the Eulerian velocity about (ξ_0, ζ_0), that is

$$U_L = u(\xi_0, \zeta_0, t) + (\xi - \xi_0)\left(\frac{\partial u}{\partial x}\right)\bigg|_{(\xi_0,\zeta_0)} + (\zeta - \zeta_0)\left(\frac{\partial u}{\partial z}\right)\bigg|_{(\xi_0,\zeta_0)} + O((ak)^2). \tag{2.9}$$

The averaged Lagrangian velocity, or drift, is then given by

$$u_L = \frac{1}{T}\int_0^T U_L\,\mathrm{d}t = (ak)^2 ce^{2k\zeta_0}, \tag{2.10}$$

where $T = 2\pi/\omega$ and the phase velocity is given by $c = g/\omega$. This is the classical Stokes drift for periodic linear deep-water surface gravity waves, and by definition $u_s \equiv u_L$.

2.2. *Linear wave packets*

In the context of the ocean, a slightly more realistic example comes from considering a compact wave packet. This follows the work of Kenyon (1969). Let

$$\eta = \int \hat{a}(k)e^{i(kx - \omega t)}\,\mathrm{d}k, \quad \phi = -i\int \frac{\hat{a}(k)}{k}\,\omega\,e^{kz}e^{i(kx - \omega t)}\,\mathrm{d}k, \tag{2.11a,b}$$

where $\hat{a}(k)$ is the amplitude density and the reality condition implies

$$\hat{a}(-k) = \hat{a}^*(k). \tag{2.12}$$

Furthermore, setting $\rho = 1$, we define the energy spectral density $F(k)$ by

$$\int F(k)\,\mathrm{d}k = \frac{g}{2}\int \eta^2(x,t)\,\mathrm{d}x = \frac{g}{2}\int |\hat{a}(k)|^2\,\mathrm{d}k, \tag{2.13}$$

where the integral is over the (compact) wave packet and the last relation is via Parseval's theorem.

The Lagrangian motion induced by this packet, found via equation (2.6), is

$$\xi - \xi_0 = \mathrm{i}\int \hat{a}(k)\mathrm{e}^{k\zeta_0}\mathrm{e}^{\mathrm{i}(k\xi_0 - \omega t)}\,\mathrm{d}k, \tag{2.14}$$

and

$$\zeta - \zeta_0 = \int \hat{a}(k)\mathrm{e}^{k\zeta_0}\mathrm{e}^{\mathrm{i}(k\xi_0 - \omega t)}\,\mathrm{d}k. \tag{2.15}$$

The Stokes drift then follows from (2.9), from which we find

$$u_L = \int \frac{k^2}{\omega}F(k)\mathrm{e}^{2k\zeta_0}\,\mathrm{d}k. \tag{2.16}$$

In the limit $F = ga_0^2\delta(k)$, we return equation (2.10). At the surface, the drift reads

$$u_{L,s}(\zeta_0 = 0) = \int \frac{k^2}{\omega}F(k)\,\mathrm{d}k. \tag{2.17}$$

This prediction is linear and does not give information about whether focusing or defocusing packets lead to greater convergence. To gain intuition about this phenomenon, in appendix B, we examine the drift associated with weakly nonlinear wave packets and find that focusing induces a positive correction to the Stokes drift while defocusing induces a negative correction. Furthermore, steep and breaking waves are not linear, so this analysis does not yield information about what happens in those cases. To gain intuition about this behaviour, we next turn to a scaling argument.

2.3. *Scaling argument for the added drift due to breaking*

In a recent paper, Pizzo (2017) examined the equation of John (1953), which is a relationship between the horizontal kinematics of a particle on the fluid surface and the free surface geometry, to derive a criterion for particles to surf an underlying wave. There, it is shown that in a localized region on the forward face of the wave, near the crest, particles accelerate and surf the underlying wave. The John equation (see also Sclavounos (2005)) is

$$\ddot{\xi} + \left\{ 2\left(\frac{\eta_x\eta_{xt}}{1 + \eta_x^2}\right)\dot{\xi} + \left(\frac{\eta_x\eta_{xx}}{1 + \eta_x^2}\right)\dot{\xi}^2 + \frac{(\eta_{tt} + g)\eta_x}{1 + \eta_x^2} \right\} = 0, \tag{2.18}$$

where again ξ is a the horizontal position of the particle.

Now, following Drazen *et al.* (2008), Loewen & Melville (1991), we assume the free surface displacement η scales with h while horizontal distances scale with the typical wavenumber k and time with the typical angular frequency ω^{-1}. Furthermore, we assume that the particle velocity increases with increasing slope, consistent with numerical (Vinje & Brevig 1981) and laboratory (Drazen *et al.* 2008) observations. Therefore, the maximum acceleration, which we denote as A_m, is given by

$$A_m = \chi(hk)g + O((hk)^2), \tag{2.19}$$

where χ is a $O(1)$ non-dimensional constant. Assuming this acceleration holds approximately over the duration of breaking, T, which we take to be $2\pi/\omega$ (Rapp & Melville 1990), we conclude

$$k\Delta x = \chi \frac{gk}{2} T^2(hk) = \chi'(hk), \tag{2.20}$$

where χ' is an order $O(10)$ constant and Δx is the total horizontal displacement. We define the slope $S = hk$, and following earlier work introduce a threshold for breaking S_0, leading to

$$k\Delta x = \chi''(S - S_0), \tag{2.21}$$

where χ'' is an order $O(10)$ constant. This can be written as a drift velocity due to breaking $u_{L,s} = \Delta x/T$, with $c = \omega/k$ the characteristic phase velocity, that is

$$u_{L,s}/c = \chi''(S - S_0). \tag{2.22}$$

As we will show later in the paper, this result is observed in our numerical results. Ultimately, this scaling should be tested in laboratory experiments. We now investigate the Lagrangian drift for non-breaking and breaking wave focusing packet by performing direct numerical simulations.

3. A numerical wave tank for breaking waves

We present a numerical configuration to model a dispersive focusing wave packet. That is, we have developed a numerical wave tank. The focusing of the waves leads to a breaking event localized in space and time in the centre of the numerical domain, similar to the laboratory experiments from Rapp & Melville (1990), Drazen *et al.* (2008) or the recent numerical simulations from Derakhti & Kirby (2014, 2016). We seed the tank with Lagrangian particles that we follow in space and time during the simulation, permitting the analysis of the Lagrangian properties of the breaking and non-breaking focusing packets.

3.1. *The Gerris flow solver*

We solve the two-dimensional two-phase incompressible Navier–Stokes equations accounting for surface tension and viscous effects using the open-source solver Gerris (Popinet 2003, 2009), based on a quad/octree adaptive spatial discretization, multilevel Poisson solver. The interface between the high density liquid (water) and the low density gas (air) is reconstructed by a geometric volume of fluid method.

The multifluid interface is traced by a function $\mathcal{T}(\boldsymbol{x}, t)$, defined as the volume fraction of a given fluid in each cell of the computational mesh. The density and

viscosity can thus be written as $\rho(\mathcal{T}) = T\rho_w + (1 - \mathcal{T})\rho_a$, $\mu(\mathcal{T}) = \mathcal{T}\mu_w + (1 - \mathcal{T})\mu_a$, with ρ_w, ρ_a and μ_w, μ_a the density and viscosity of the two fluids (water and air), respectively. The incompressible, variable density, Navier–Stokes equations with surface tension can be written as

$$\left.\begin{array}{r}\rho(\partial_t \boldsymbol{u} + (\boldsymbol{u} \cdot \boldsymbol{\nabla})\boldsymbol{u}) = -\boldsymbol{\nabla}p + \boldsymbol{\nabla} \cdot (2\mu\boldsymbol{D}) + \gamma\kappa\delta_s\boldsymbol{n}, \\ \partial_t\rho + \boldsymbol{\nabla} \cdot (\rho\boldsymbol{u}) = 0, \\ \boldsymbol{\nabla} \cdot \boldsymbol{u} = 0, \end{array}\right\} \tag{3.1}$$

with $\boldsymbol{u} = (u, w)$ the fluid velocity, $\rho \equiv \rho(\boldsymbol{x}, t)$ the fluid density, $\mu \equiv \mu(\boldsymbol{x}, t)$ the dynamic viscosity and $\boldsymbol{D}$ the deformation tensor defined as $D_{ij} \equiv (\partial_i u_j + \partial_j u_i)/2$. The Dirac delta, δ_s applied on the surface only, expresses the fact that the surface tension term is concentrated on the interface, where γ is the surface tension coefficient, κ and $\boldsymbol{n}$ the curvature and normal to the interface, respectively.

The density and viscosity ratios of the two phases are those of air and water. The surface tension is $\gamma = 0.07$ N m^{-1}, corresponding to the surface tension between air and water. The Reynolds number in the liquid is defined by $Re = c\lambda/\nu$, with c the linear deep-water gravity wave central phase speed of the wave packet (see below) and ν the kinematic viscosity of the liquid (water). Due to computational limitations, related to spatial resolution constraints, we limit ourselves to $Re = 40\,000$. This resolves the viscous boundary layer at the surface, and is still a large Reynolds number. However, it is smaller than the $O(10^6)$ Reynolds number corresponding to waves generated in the laboratory. Nevertheless, we have shown in previous work on energy dissipation, air entrainment and the breaking-induced currents that this lower Reynolds number still leads to consistent results with laboratory studies, implying that the Reynolds number is sufficient to describe the phenomena in question (Deike *et al.* 2015, 2016; Pizzo *et al.* 2016). This gives us confidence in studying the Lagrangian transport in the breaking-induced flow in this paper.

Note that we are performing direct numerical simulations (DNS) of the Navier–Stokes equations to solve for breaking waves, therefore no model or assumption is used in our computations. There is simply a limitation in the Reynolds number we can achieve with the molecular viscosity. This DNS approach should not be confused with other approaches to model breaking wave dissipation using a turbulent model, such as an eddy viscosity, which rely on laboratory experiment to calibrate the value of the eddy viscosity. Tian *et al.* (2010), Tian, Perlin & Choi (2012) used an eddy viscosity between 0.5×10^{-3} and 1.7×10^{-3} m^2 s^{-1} to reproduce the dissipation rate observed in their breaking wave experiments. This would lead to a Reynolds number between 2×10^3 and 8×10^3, between five to twenty times smaller than the Reynolds number we consider using the molecular diffusivity.

The present solver has been successfully used in multiphase problems like atomization (Fuster *et al.* 2009; Tomar *et al.* 2010), the growth of instabilities at the interface (Fuster *et al.* 2013) and the nonlinear dynamics of wave breaking in two (Deike *et al.* 2015; Pizzo *et al.* 2016) and three dimensions (Deike *et al.* 2016). These previous studies have validated these methods and shown the ability of the numerical simulations to reproduce properties observed in the laboratory regarding capillary effects on wave breaking (Deike *et al.* 2015), wave dissipation due to breaking (Deike *et al.* 2015, 2016), air entrainment and bubble statistics in breaking waves (Deike *et al.* 2016), as well as current generation (Pizzo *et al.* 2016).

3.2. *The focusing wave packet configuration*

The numerical wave tank is $L = 32$ m long and $l = 2$ m high, with a water depth of $d = 1$ m. Top and bottom boundary conditions are no slip. The left-hand side of the tank corresponds to the numerical wave maker and consists of a forcing boundary condition on the velocity ($u(x = 0, t)$, $w(x = 0, t)$) and on the interface $\eta(x = 0, t)$. Following laboratory experiments, we consider a focusing wave packet to create breaking waves (Rapp & Melville 1990; Drazen *et al.* 2008) and the imposed boundary conditions at $x = 0$ are

$$\left.\begin{aligned}
\eta(x = 0, t) &= \sum_{i=1}^{N} a_i \cos[\omega_i(t - t_b) - k_i(x - x_b)], \\
u(x = 0, t) &= \frac{\partial \phi}{\partial x} \quad \text{and} \quad w(x = 0, t) = \frac{\partial \phi}{\partial z}, \quad \text{with} \\
\phi(x, z) &= \sum_{i=1}^{N} \frac{a_i \omega_i}{k_i} \frac{\cosh(k_n(z + d))}{\cosh(k_n d)} \sin[\omega_i(t - t_b) - k_i(x - x_b)].
\end{aligned}\right\} \quad (3.2)$$

The linear prediction of the focusing time and location are $t_b = 25$ s and $x_b = 12$ m, in the middle of the tank. Following Rapp & Melville (1990), Drazen *et al.* (2008), we consider packets with $N = 32$ components, a central frequency $f_c = 0.89$ Hz (corresponding to a central wavelength $\lambda_c = 2\pi/k_c = 1.9$ m which is found using the linear dispersion relation for gravity waves, $\omega^2 = gk \tanh(kd)$) and a bandwidth $\Delta = \Delta f/f_c = 0.75$. We use the constant slope formulation (Drazen *et al.* 2008) with $s = a_i k_i$ constant for all components. The maximum linear slope at focusing is then given by

$$S = \sum_{i=1}^{N} a_i k_i = Ns. \quad (3.3)$$

The central phase speed of the wave packet is $c = \omega_c/k_c$. For a non-breaking packet, the theoretical Stokes drift of the packet can be computed combining equation (2.16) and the initial shape of the packet given by (3.2).

The last 12 m of the tank is a numerical sponge layer, based on the one developed by Clement (1995) for a potential solver. This consists of an added empirical friction term which acts to attenuate the velocity. This leads to almost complete suppression of waves propagating towards the right end of the numerical tank. The transition between the physical part of the tank (the first 24 m) and the sponge layer (the last 12 m) is smooth to avoid wave reflections. Finally the end of the tank on the right corresponds to a wave radiation boundary condition, in order to remove any remaining small perturbations.

Adaptive mesh refinement is used to accurately solve for the interface and the vortical structures. We tested several resolutions and adaptive grid configurations and report in this paper on high and medium resolution configurations. The equivalent grid resolution for the high resolution case is a mesh size of $\delta_{h,i} = 1$ mm on the interface gradients and $\delta_{h,v} = 4$ mm on the vortical structure in the air or water, and the medium resolution has a mesh of $\delta_{m,i} = 2$ mm on the interface gradients and $\delta_{m,v} = 8$ mm on the vortical structure. As will be discussed below, we observed convergence of the results for the total dissipation and total drift between these two resolutions. Note, although we are solving for some effects due to surface tension (the capillary length scale for air–water is $l_{gc} = \sqrt{\gamma/(\rho g)} \approx 3$ mm, and the corresponding wavelength is

$\lambda_{gc} = 2\pi l_{gc} \approx 1$ cm), we do not fully resolve the dynamics of micro-breakers and parasitic capillaries, for which a higher resolution is needed (around 0.2 mm was successfully used for parasitic capillaries in Deike *et al.* (2015) for example).

The flow is seeded by Lagrangian particles that are systematically tracked. Each Lagrangian particle i is described by its Lagrangian trajectory $\{x_i(t), z_i(t)\}$, or velocity $\{u_i(t), w_i(t)\}$. The initial location of the particles is denoted by $\{x_i(t=0), z_i(t=0)\} = \{x_{i,0}, z_{i,0}\}$. The flow is seeded with one particle every 10 cm horizontally, i.e. $x_{i+1,0} - x_{i,0} = 10$ cm; and 1 particle every 1 cm vertically, i.e. $z_{i+1,0} - z_{i,0} = 1$ cm, leading to a total of over 30 000 Lagrangian particles over the tank. We mainly focus our analysis on the Lagrangian kinematics in an area around the focusing point of the wave packet. The accuracy of the tracking scheme has been tested in Tomar *et al.* (2010) and has been verified in our case for propagating waves by comparing the Lagrangian drift for a monochromatic small amplitude wave against the theoretical Stokes drift. The test case is presented in the appendix A and we found very good agreement between the simulation and the theory.

3.3. *Wave focusing, breaking and energy dissipation due to breaking*

Figure 1(*a*) shows the space–time evolution of the free surface displacement $\eta(x, t)$ for a typical numerical experiment of a focusing wave packet leading to breaking. The packet is generated at the left side of the tank and focuses around $x \approx 12$ m and $t \approx 25$ s, as expected by linear theory and in agreement with laboratory experiments (Rapp & Melville 1990; Drazen *et al.* 2008). The wave packet propagates at the weighted group velocity as observed experimentally (Drazen *et al.* 2008; Tian *et al.* 2010, see also Pizzo 2015, Pizzo & Melville 2016), $c_{gs} = (\sum_{i=1}^{N} a_i^2 c_{gi})/(\sum_{i=1}^{N} a_i^2)$, where $c_{gi} = \partial \omega_i / \partial k_i$ is the group velocity of the wave component. The wave breaks close to the focusing point, with some waves being radiated back towards the left boundary of the tank. The packet then continues to propagate and defocuses, before being damped when it reaches the numerical beach ($x > 24$ m), and no wave signal is visible for $x > 30$ m. No reflection is visible on the right-hand side of the tank.

Note, convergence of the dynamical and integrated quantities such as the time and location of focusing, the total wave dissipation, and average drift of patches of particles have been verified between the medium and high resolutions.

Figure 1(*b*) shows the breaking parameter b as a function of the wave slope S. The breaking parameter b is related to the dissipation rate per unit length of breaking crest ϵ_l by (Duncan 1981; Phillips 1985)

$$\epsilon_l = b\rho c^5/g \tag{3.4}$$

and is computed from the dissipation due to breaking as in Drazen *et al.* (2008), by computing the wave energy budget before and after breaking. Excellent agreement is found between our numerical results in the present configuration and earlier laboratory work (Drazen *et al.* 2008; Romero *et al.* 2012; Grare *et al.* 2013), the inertial argument from Drazen *et al.* (2008) and recent numerical simulations (Deike *et al.* 2015, 2016; Derakhti & Kirby 2016; Pizzo *et al.* 2016). The breaking threshold observed in our present configuration is $S_* = 0.31$, where breaking is defined by the appearance of a vertical interface, which is a classic geometric criterion (Perlin *et al.* 2013; Deike *et al.* 2015). This relatively high value is probably related to the limited mesh size which does not allow the proper resolution for parasitic capillaries and micro-breaking processes.
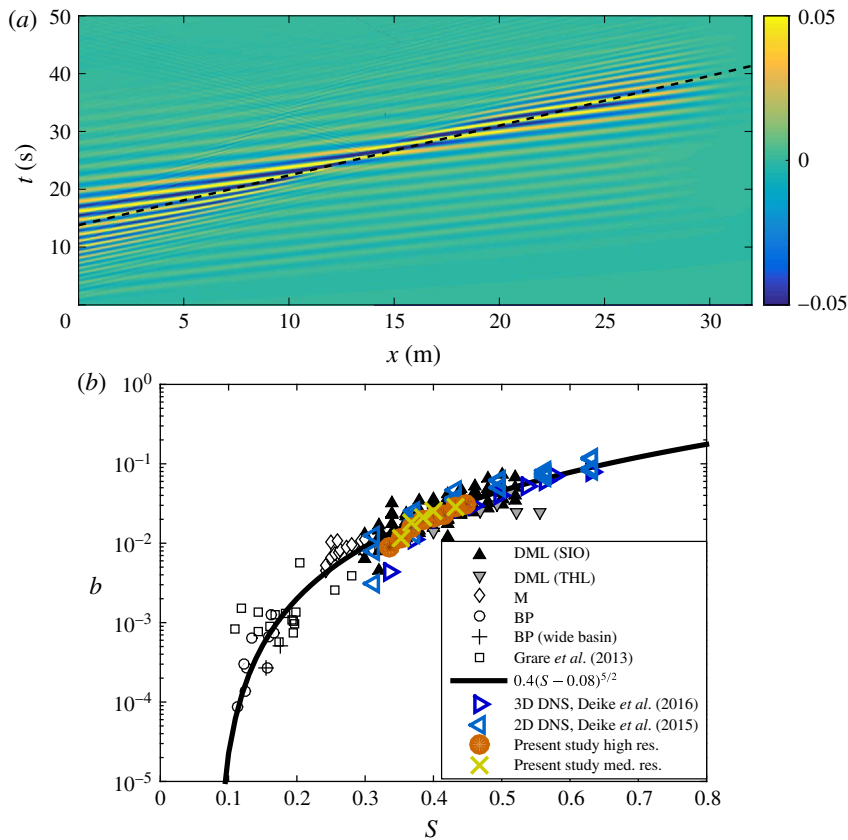
FIGURE 1. (Colour online) (*a*) Space–time diagram of the wave height $\eta(x, t)$, showing the propagation and focusing of the wave packet, for $S = 0.38$, $f_c = 0.89$ Hz, $\Delta f / f_c = 0.75$. Breaking occurs at $t \approx 25$ s and at $x \approx 12$ m. Colour scale is $\eta(x, t)$ in metres. The dashed line is the energy weighted group velocity c_{gs} defined by Drazen *et al.* (2008), that describes the propagation of the wave packet. No significant reflection can be seen at the right end of the numerical tank due to the numerical sponge layer. (*b*) Breaking parameter b as a function of wave slope S, for the high resolution (full circle) and medium resolution (cross) runs. The present simulations are in agreement with earlier experimental and numerical work as well as the inertial scaling argument from Drazen *et al.* (2008), Romero *et al.* (2012). Laboratory data are from Melville (1994) (M), Banner & Peirson (2007) (BP), Drazen *et al.* (2008) (DML), Grare *et al.* (2013) and numerical data from Deike *et al.* (2015, 2016).

The mass in each fluids (air and water) is conserved to better than 0.2 % as shown in appendix A.

The results in the remainder of the paper are normalized by the characteristic wavenumber k_c, angular frequency ω_c and phase velocity c, all taken as the central component of the wave packets. For dynamical quantities, such as the group velocity or the wave energy, the weighted quantities (e.g. the weighted group velocity) arise naturally (Pizzo 2015) and provide a better non-dimensionsalization of the variables (Drazen *et al.* 2008; Tian *et al.* 2010). However, for the present study, the kinematics of the wave is considered and the weighted quantities do not arise naturally in the

theoretical analysis which justifies our choice to work with the central wave packet quantities. Note that all results on the drift presented in § 4 are not modified if we were to use weighted quantities, as the characteristic scales are only used for normalization.

4. Lagrangian displacement of particles under focusing packets: non-breaking and breaking cases

In this section, we discuss the Lagrangian kinematics of breaking and non-breaking wave packets and compute the horizontal drift.

4.1. *Particle trajectories*

Figures 2 and 3 show the spatial wave surface $\eta(x, t)$ at different times t before and after breaking. The propagation and focusing of the wave packet close to the focusing point is visible, in time and space, for a non-breaking case (figure 2, $S = 0.26$) and a breaking case (figure 3, slope $S = 0.38$). These results are representative of our breaking and non-breaking cases. The horizontal axis x is centred by the linear focusing location x_b and normalized by the central wavenumber, $(x - x_b)k_c$, the vertical axis is normalized to zk_c, while the time is centred by the linear focusing time t_b and normalized by the central angular frequency ω_c to be $(t - t_b)\omega_c$.

Focusing occurs within one wave period $1/f_c = 2\pi/\omega_c$ of the linear focusing time t_b, and close to the linear focusing location x_b, and is consistent with observations in laboratory experiments (Rapp & Melville 1990; Drazen *et al.* 2008). Together with the free surface, these figures also show the displacement of particles $\{x_i(t), z_i(t)\}$, at different initial depths ($z_{i,0} = 0k_c$, $-0.64k_c$ and $-1.28k_c$), and initial horizontal locations upstream ($(x_{i,0} - x_b)k_c = -2.9k_c$), near ($(x_{i,0} - x_b)k_c = 1.3k_c$) and downstream ($(x_{i,0} - x_b)k_c = 8k_c$) of the focusing point.

Figure 2 shows a typical non-breaking focusing case (central frequency $f_c = 0.89$ Hz, bandwidth $\Delta f/f_c = 0.76$ and maximum linear slope $S = 0.26$). The wave reaches its largest slope near the focusing point. The trajectories of the particles at the surface are similar in all non-breaking cases and can be described as follows: small deviations to almost closed ellipses before the focusing time and the arrival of the main part of the wave packet. These small amplitude oscillations correspond to waves of small amplitude arriving before focusing. During focusing, a significant horizontal jump, or drift in the horizontal x-direction is observed, and corresponds to the passing of the wave group. The total horizontal displacement during the whole simulation is almost entirely due to this event and it corresponds to the horizontal transport, similar to the Stokes drift described for a single frequency propagating wave. The horizontal velocity of the particles u at the surface at the focusing time are $u/c \approx 0.2$, where c is the central phase speed of the wave packet. After focusing, small oscillations are visible again, with much smaller velocities. Next, the depth dependence is characterized by the same behaviour, with an amplitude that is attenuated by an exponential decay with e-folding scale corresponding to twice the wavenumber. Finally the particles close to the bottom of the tank experience a negative drift (a displacement opposite to the wave propagation), corresponding to the return flow, consistent with mass conservation (Longuet-Higgins 1953).

Figure 3 shows a typical focusing packet leading to breaking (central frequency $f_c = 0.89$ Hz, bandwidth $\Delta f/f_c = 0.76$ and maximum linear slope $S = 0.38$). The focusing of wave energy leads to breaking and the impact of the jet occurs at $t \approx t_b$. The displacement of the particles at the surface that are located far enough downstream
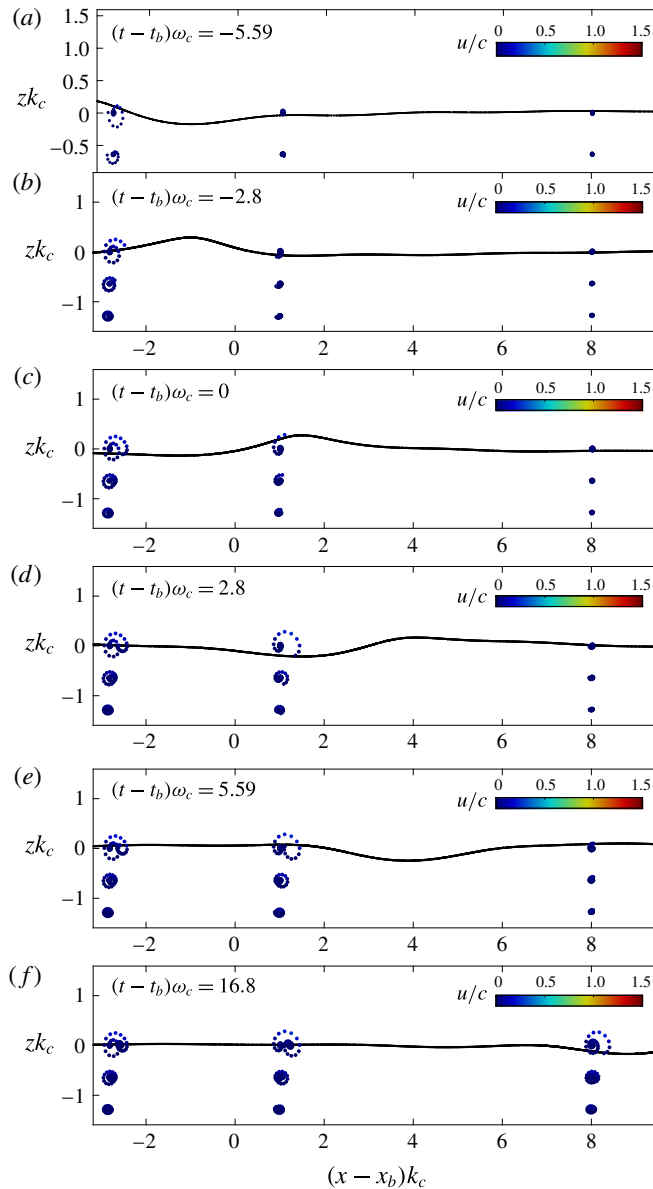
FIGURE 2. (Colour online) Interface evolution $\eta(x, t)$ and particle trajectories during wave propagation for a non-breaking focusing packet, $f_c = 0.89$ Hz ($k_c = 5.58$ rad m^{-1}), $\Delta f/f_c = 0.76$ and maximum linear slope $S = 0.26$. The interface $\eta(x, t)$ is shown in black, while the particle trajectories are colour coded by their horizontal velocity u/c. Times between $(t - t_b)\omega_c = -5.59$ before focusing (*a*) and $(t - t_b)\omega_c = 16.8$ after focusing (*f*) are shown. Focusing occurs at $t \approx t_b$, with particles presenting a larger drift and velocity at that time. The drift of all particles is similar for all particles at the same depth and decreases with depth. Note that particle trajectories shown here above the interface are in fact particles at the interface but for earlier times.
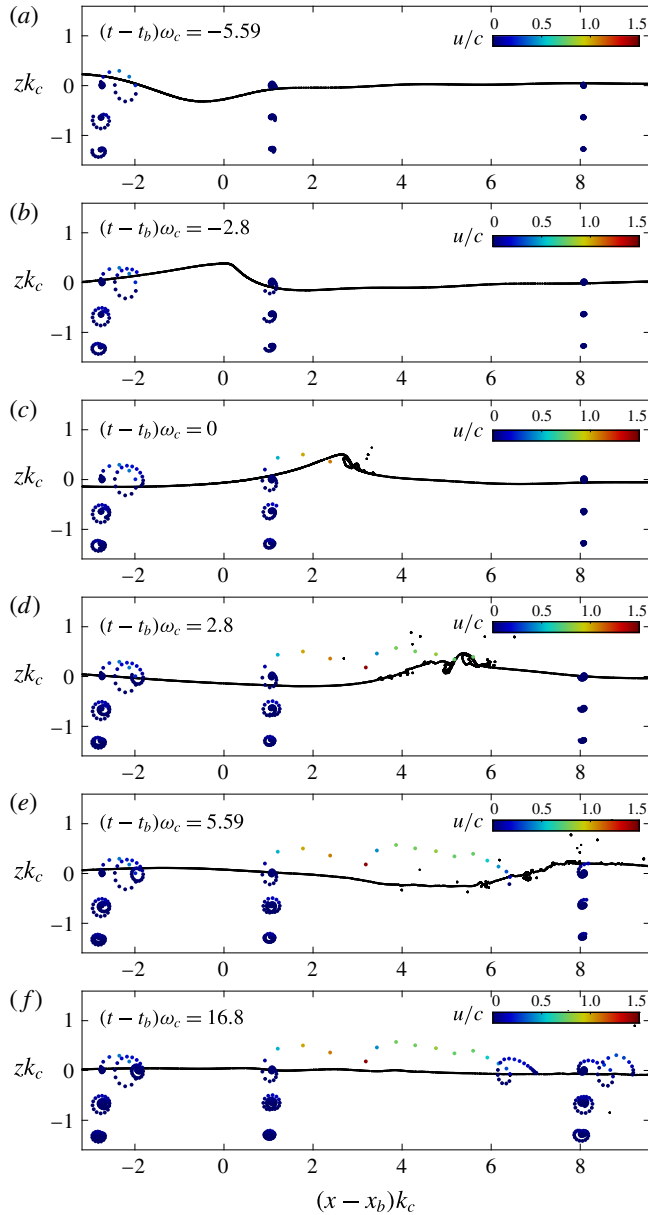
FIGURE 3. (Colour online) Interface evolution and particle trajectories during the wave propagation and wave breaking event for a focusing packet, $f_c = 0.89$ Hz ($k_c = 5.58$ rad m^{-1}), $\Delta f/f_c = 0.76$ and maximum linear slope $S = 0.38$. The interface $\eta(x, t)$ is in black, while the particle trajectories are colour coded by their horizontal velocity u/c. Times between $(t - t_b)\omega_c = -5.59$ before breaking (*a*) and $(t - t_b)\omega_c = 16.8$ after breaking (*f*) are shown. Breaking occurs at $t \approx t_b$, with particles presenting a much larger drift and velocity. The drift decreases with depth. Note that particle trajectories shown here above the interface are in fact particles at the interface but for earlier times.

of the focusing breaking point is similar to that discussed above for a non-breaking focusing packet: small oscillations before the focusing event, with small velocities ($u/c < 0.1$) and a small jump when the main packet passes with a velocity $u/c \approx 0.4$. The net drift is therefore larger in the horizontal direction than for the non-breaking case, even out of the breaking point, due to the increase in the wave amplitude (or slope). A similar picture is visible for particles far enough upstream of the breaking point. Again, almost all the drift of the particles happens during a short period around focusing (typically one central wave period $1/f_c$); the displacement before and after being small compared to the jump when the focused wave passes by. The amplitude of the displacement decreases with depth for the particles away from the breaking area in a similar way to what we described for the non-breaking packet.

By comparison, the particles located close to the breaking point experience a large jump, or drift in the propagation direction during the breaking event, with a displacement that can be larger than one meter, i.e. of the order of λ_c. The velocity of the particles at breaking can be above the central phase velocity c (Vinje & Brevig 1981; Pizzo 2017), with a value of $1.1c$ when the particle catches the breaker, and up to $1.5c$ during splashes for the particular example displayed here. This displacement is therefore an order of magnitude larger than for non-breaking particles at the focusing point, or for particles away from the breaking point. This corresponds to a Lagrangian transport due to the breaking wave which is the central point of this paper. Note also, particles can be transported vertically (downward) in the water when located around the breaking area corresponding to the vertical transport of horizontal momentum (Rapp & Melville 1990; Drazen & Melville 2009).

Particles located deeper in the water experience a smaller displacement in the propagation direction when located in the upper half of the tank and a negative displacement in the lower half of the tank, corresponding to the return flow, again consistent with mass conservation.

4.2. *Drift at the surface*

We now discuss the displacement of particles at the surface. Figure 4 shows the trajectories of such particles located just before, at, and just after the focusing point for a non-breaking and a breaking focusing packet, with the time colour coded.

As already described above, in the non-breaking case, all trajectories are similar, with small oscillations before the focusing time, and a small jump at focusing in the propagation direction. The net drift in the propagation direction is between $0.05\lambda_c$ and $0.1\lambda_c$, for all particles at the surface. This observation applies over a wide area around the focusing point, where the horizontal extent of the initial particle positions is given by $-2 < (x_0 - x_b)k_c < 10$, i.e. over approximately $2\lambda_c$. The particles initially near the focus point experience a slightly larger drift due to focusing which is explained by the weakly nonlinear theory presented in appendix B, where the focusing effect induces a positive correction to the classical Stokes drift. This effect increases with the wave slope S, as suggested theoretically.

In the breaking case, particles initially in a narrow window around the effective breaking point (in this case close to $(x - x_b)k_c \approx 1$) experience a much larger displacement (drift) in the propagation direction, than those located further upstream or downstream. The particle located at $(x_0 - x_b)k_c = -1.9$ moves only $0.06\lambda_c$, while that at $(x_0 - x_b)k_c = -0.3$ moves around $0.2\lambda_c$. The one at $(x_0 - x_b)k_c = 1.3$ is caught by the breaking wave and moves around $0.36\lambda_c$, and finally the one slightly further at $(x_0 - x_b)k_c = 1.6$ moves almost $1\lambda_c$, surfing the wave. Particles much further
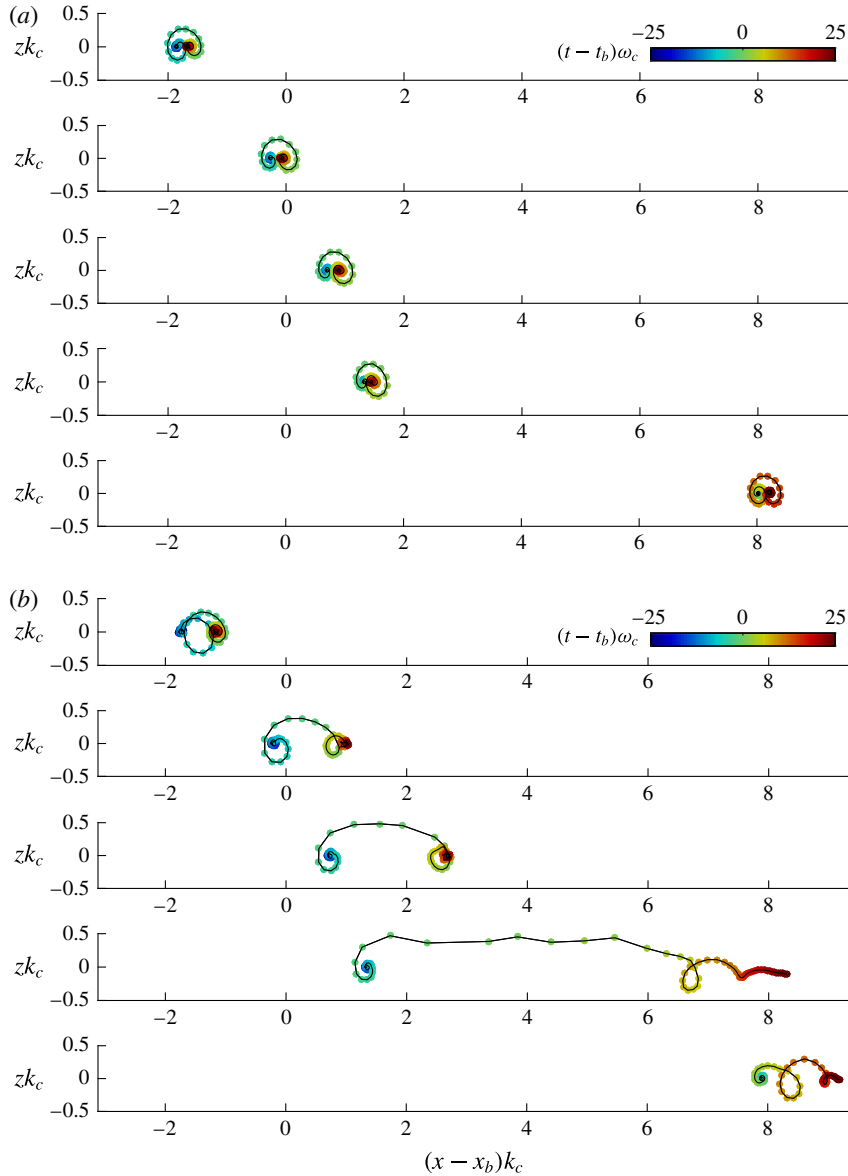
FIGURE 4. (Colour online) Trajectories of particles for focusing packets, close to focusing (*a*) no breaking and close to breaking (*b*) breaking. $f_c = 0.89$ Hz, bandwidth $\Delta f / f_c = 0.76$. $S = 0.26$ for the non-breaking packet and $S = 0.38$ for the breaking packet. Particles just before the break point do not catch the wave, and experience a net drift smaller than the ones that are catching the breaking wave. Finally, particles further upstream or downstream of the breaking event are not significantly influenced by breaking.

downstream have a smaller drift. This breaking case shows differences of an order of magnitude for the drift of particles located in a window of length less than one λ_c; illustrating the importance of the local effect of breaking on the drift. This effect has been recently discussed theoretically by Pizzo (2017). The drift due to breaking

is found to be an order of magnitude larger than the drift for a non-breaking packet, consistent with the scaling argument presented in §2 for the drift due to the breaking event.

As discussed previously, most of the displacement occurs within a space–time window related to the passing of the focused wave, and scaled on the characteristic wavelength and period of the wave packet. This is even more dramatic in the breaking case, where the acceleration is very strong during breaking.

4.3. *Spatial dependence of the total drift*

We now focus on the total horizontal drift of the particles. We define the total drift as $\Delta x(x_0, z_0) = (x_i(t_f) - x_i(t_0))$, where t_f is a time long after breaking, $(t_f - t_b)\omega_c \gg 1$ (typically the final time of the simulation), and t_0 is the initial time, long before breaking, $(t_0 - t_b)\omega_c \ll -1$ (typically the initial time of the simulation). The total drift is not sensitive to the choice of t_f, t_0, as long as the conditions $(t_0 - t_b)\omega_c \ll -1$ and $(t_f - t_b)\omega_c \gg 1$ are fulfilled. For example, the drift obtained for $(t_f - t_b)\omega_c = 56$ and $(t_f - t_b)\omega_c = 27$ (with $(t_0 - t_b)\omega_c = -140$) varies by less than 5 %.

Figure 5(*a*) shows the total drift at the surface normalized by the central wavelength, $\Delta x(x_0, z_0 = 0)/\lambda_c$, as a function of the normalized horizontal initial position $(x_0 - x_b)k_c$ for a typical breaking event ($S = 0.38$), both the raw data Δx, each data point corresponding to one particle, as well as a running average drift $\overline{\Delta x}(x_0)$ as a solid line (with the horizontal averaging window taken to be the characteristic wavelength λ_c). The drift is small far upstream and downstream of the breaking area and increases strongly near the focusing point, before decreasing again after the focusing point. The extent of the breaking area is approximately given by the central wavelength of the packet λ_c. The location $x_{b,n}$ is defined as the peak location of the drift (found to be slightly after x_b in this case), with the horizontal dashed line on the figure showing the area $[x_{b,n} - \lambda_c/2 : x_{b,n} + \lambda_c/2]$.

Figure 5(*b*) shows the normalized drift $\overline{\Delta x}/\lambda_c$, as a function of $(x_0 - x_b)k_c$, for increasing slopes, for both non-breaking and breaking focusing wave packets. For each case, the maximum location is extracted, $x_{b,n}(S)$, and the breaking area, $[x_{b,n} - \lambda_c/2 : x_{b,n} + \lambda_c/2]$, is indicated by horizontal dashed lines. For smaller slopes, the drift at the surface is almost constant as a function of the horizontal position ($S < 0.2$). For intermediate slopes of non-breaking wave packets ($0.2 < S < 0.31$), a significant increase of the drift around the focusing location is observed. This is again in agreement with the argument discussed earlier for weakly nonlinear packets (appendix B). The breaking cases exhibit a strong increase in the horizontal drift around the breaking area. The breaking location defined as the location of the maximum drift $x_{b,n}$ generally moves upstream as the slope S increases, which is consistent with earlier reports on breaking waves by focusing packets (Rapp & Melville 1990). The width of the region of enhanced drift increases with the slope, i.e. enhanced breaking strength leads to a larger area of enhanced drift.

4.4. *Vertical profiles at the focusing point*

We now look at the vertical profile of the horizontal drift. We compute the horizontally averaged displacement $\langle \overline{\Delta x}(z_0) \rangle$, for particles initially located at $z_{i,0} = z_0$, and within the horizontal breaking area defined previously, i.e. particles initially located between $x_{b,n} - \lambda_c/2$ and $x_{b,n} + \lambda_c/2$.

To facilitate the comparison with the Stokes drift velocity defined in §2 and in the literature, we now define the drift velocity $u_L(z_0)$, with T the typical time of the wave
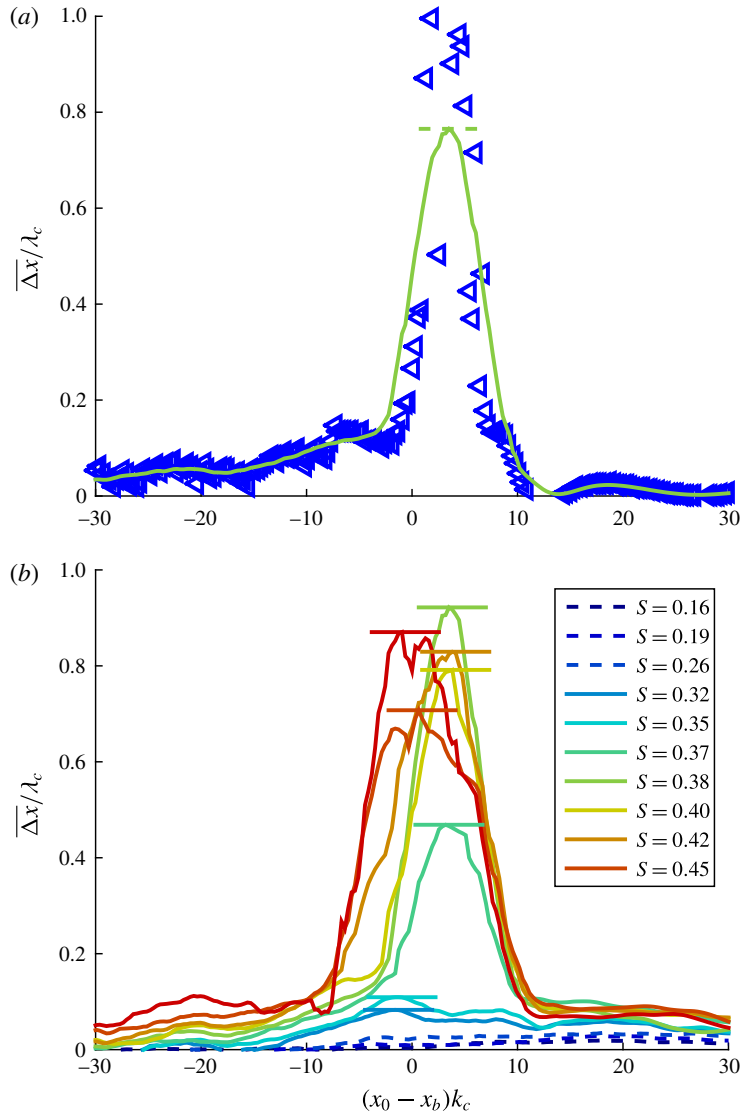
FIGURE 5. (Colour online) (*a*) Total horizontal drift for particles initially at the surface, $z_0 = 0$, normalized by the central wavelength λ_c, for a breaking case ($S = 0.38$) as a function of the normalized initial horizontal position of the particles $(x_0 - x_b)k_c$. Triangles are the raw data $\Delta x(z_0)$, while the solid line, $\overline{\Delta x(z_0)}$, is obtained after a running mean averaged over λ_c. The breaking or focusing point $x_{b,n}$ is taken as the maximum drift location for each case, and the horizontal dashed line indicates the breaking area, $[x_{b,n} - \lambda_c/2 : x_{b,n} + \lambda_c/2]$. The area of breaking is where particles experience a stronger drift due to breaking and will be used to compute vertical profiles and drift at the surface. (*b*) $\overline{\Delta x(z_0)}/\lambda_c$ as a function of $(x_0 - x_b)k_c$ and wave slope, including breaking and non-breaking packets. Non-breaking cases are indicated by dashed lines while breaking cases are solid lines. Breaking threshold in these simulations is $S = 0.31$, clearly separating the horizontal profiles. For each case, the horizontal solid line indicates the breaking area, $[x_{b,n} - \lambda_c/2 : x_{b,n} + \lambda_c/2]$. The width of the region of enhanced drift increases with the slope, while $x_{b,n}$ decreases as S increases.
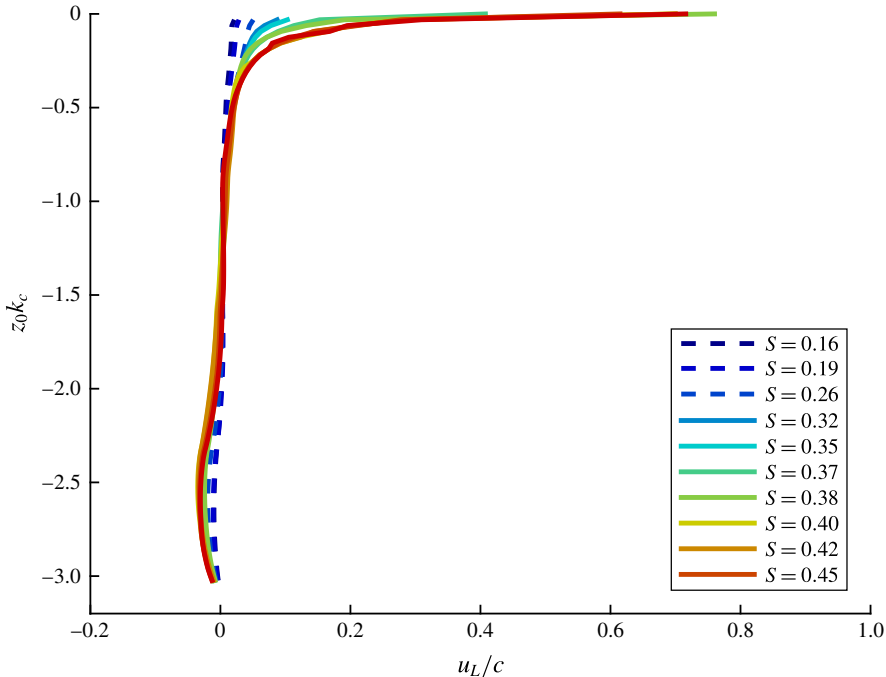
FIGURE 6. (Colour online) Vertical profiles of the normalized horizontal particle drift $u_L/c = \langle \overline{\Delta x} \rangle / \lambda_c$, as a function of the initial depth of the particles $z_0 k_c$, obtained for each depth by averaging over a horizontal window $x \in [x_{b,n} - \lambda_c/2 : x_{b,n} + \lambda_c/2]$ around the maximum drift location $x_{b,n}$, for increasing slope S (from blue to red). The drift at the surface increases with the slope, as does the return flow in the bottom half of the tank, ensuring mass conservation. Non-breaking cases are indicated by dashed lines while breaking cases are solid lines.

packet, taken as $T = 1/f_c = 2\pi/\omega_c$,

$$u_L(z_0) = \frac{\langle \overline{\Delta x}(z_0) \rangle}{T}. \tag{4.1}$$

Note that $u_L(z_0)/c = \langle \overline{\Delta x}(z_0) \rangle / (\lambda_c)$.

Figure 6 shows the normalized vertical profiles of the horizontal drift $u_L(z_0)/c$, for increasing wave slope S, from small amplitude non-breaking packets (in blue) to stronger breaking waves (in red). The drift near the surface in the propagation direction increases significantly with the wave slope. The increase in the drift at the surface is further enhanced until we reach the breaking threshold ($S > 0.31$ here) where the drift shows a strong increase. It corresponds to the added Lagrangian transport due to breaking. This added drift due to breaking increases with the breaking strength. Moreover, a return flow is observed in the bottom part of the tank (extending from the bottom a distance $0.2\lambda_c$, or $0.4d$), with an intensity increasing with the slope. This return flow balances the downstream drift near the surface assuring mass conservation. Note that we have verified that $\int \langle \overline{\Delta x}(z_0) \rangle \, dz_0 = 0$, and that mass is indeed conserved, up to $0.2\,\%$ (as discussed in the appendix A for the total mass budget).

The general shape of the profile does not change significantly if the running averaging window is increased or reduced by a factor of 2; however, the magnitudes
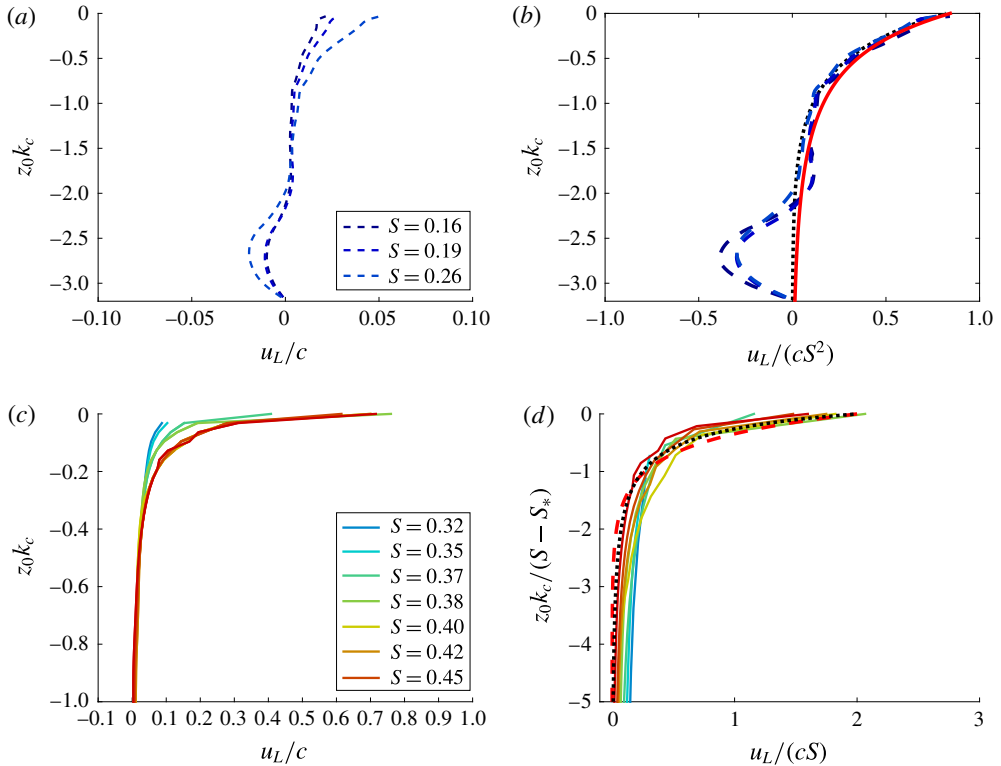
FIGURE 7. (Colour online) Rescaled vertical profiles of the particle drift velocity, averaged over a horizontal window $x \in [x_{b,n} - \lambda_c/2 : x_{b,n} + \lambda_c/2]$, for increasing slope S. Slope is colour coded (same as in figure 6). (a,b) Rescaling of the non-breaking wave packet, showing $z_0 k_c$ in the y-axis and u_L/c (a) and $u_L/(cS^2)$ (b) in the x-axis. The S^2 scaling for the drift at the surface is observed. Dashed line is $u_L/c = \chi_1 S^2 e^{-2k_c z_0}$ with $\chi_1 = 0.82$ obtained from (2.17). Solid line is the linear theory given by (2.16). A reasonable collapse of all data onto the theoretical curve is observed, the e-folding scale is then $1/2k_c$. (c,d) Rescaling of the breaking packets. (c) u_L/c in x-axis as a function of $z_0 k_c$ in y-axis. (d) u_L/cS in x-axis as a function of $z_0 k_c/(S - S_*)$ in y-axis. Better rescaling of the data is observed in (d), showing that the vertical scale is given by $(S - S_*)/k_c$, i.e. the height above the breaking threshold, while the drift at the surface also scales with S. Dashed line is an exponential fit, $u_L/cS = \iota_1 \exp[\iota_2(z_0 k_c)/(S - S_*)]$, with $\iota_1 = 2$, $\iota_2 = 2$ fitted constant, and dotted line is an algebraic decay $u_L/cS = \iota_3/[1 - (z_0 k_c)/(S - S_*)]^{\iota_4}$, with $\iota_3 = 2$ and $\iota_4 = 3$ fitted constants.

of both the drift at the surface and the return flow as the bottom are increased and reduced, respectively, since the averaging process gives more or less weight to the enhancement at the breaking point. The choice of a window of λ_c appears to be the most consistent choice since it corresponds to the phase averaging used to compute the classical Stokes drift.

Figure 7 shows the rescaled vertical profiles of the horizontal velocity u_L/c, with c the characteristic phase velocity of the packet, as a function of the rescaled depth $z_0 k_c$.

Figure 7(a) shows the normalized Lagrangian drift u_L/c as a function of $z_0 k_c$. The drift near the surface increases with the square of the slope S^2 and is well described

by an exponential decay with depth. Figure 7(*b*) shows the drift velocity rescaled by the slope squared, as suggested by the Stokes drift $u_L/(cS^2)$. All data in the upper part ($z_0 k_c > -2$) of the tank collapse reasonably well on a single exponential profile. The solid line corresponds to the theoretical prediction given by (2.16), where the amplitude of each wave component was computed using the initial wave packet given by (3.2). Good agreement is observed between the numerical data and the theoretical profile, with a slight deviation observed for the largest non-breaking slope considered here, which might be related to nonlinear effects. The dashed line corresponds to an exponential decay $\chi_1 S^2 c e^{-2k_c z_0}$, where $\chi_1 = 0.82$ is obtained from the Stokes drift at the surface, equation (2.17), where the amplitude of each wave component was computed using the initial wave packet given by (3.2). This simplified equation characterizes the bulk scale behaviour of the data, showing that the e-folding scale is given by the inverse of twice the characteristic wavenumber $1/2k_c$ for the non-breaking packets.

The dependency of the drift with S^2 at the surface and the e-folding scale $1/2k_c$ are no longer valid once the wave breaks, and the data are no longer described by this model. Figure 7(*c*,*d*) shows the breaking cases. In figure 7(*c*) u_L/c is shown as a function of $k_c z_0$, with the drift at the surface increasing with the slope S. Figure 7(*d*) shows u_L/cS as a function of $k_c z_0/(S - S_*)$, where $S_* = 0.31$ is the breaking threshold in the present configuration. The typical vertical scale of the profile is now $k_c/(S - S_*)$, i.e. the height above the breaking threshold, while the drift at the surface scales (and increases) with S. All data can be reasonably described by a single curve. The scaled profile can be described by an exponential fit, with $(S - S_*)/k_c$ the e-folding scale, $u_L/cS = \iota_1 \exp[\iota_2 (z_0 k_c)/(S - S_*)]$ or by an algebraic decay with depth, with the same characteristic vertical length scale, $u_L/cS = u_L/cS = \iota_3/[1 - (z_0 k_c)/(S - S_*)]^{\iota_4}$, where $\iota_{1,2,3,4}$ are fitted constant. The latter gives a slightly more accurate vertical profile. Note that in the vicinity of the surface, the drift can be described by a linear decay with depth, which arises naturally from a Taylor expansion of the previous formula (i.e. for $(z_0 k_c)/(S - S_*) \ll 1$), $u_L/cS = \iota_3/[1 - (z_0 k_c)/(S - S_*)]^{\iota_4} \approx \iota_3[1 + \iota_4 (z_0 k_c)/(S - S_*)]$. Furthermore this leads to $u_L(z_0 \approx 0)/c \approx \iota_4 S$, at first order, which is compatible with the scaling argument developed in §2.

Thus, the characteristic vertical length scale in the breaking cases is given by the height of the breaking wave (above the threshold for breaking). This is consistent with the laboratory work from Rapp & Melville (1990) that shows that the depth of the broken fluid scales with the wave height. This further shows that the nature of the Lagrangian kinematics and transport is changed when we move from non-breaking to breaking waves. The fact that the drift due to breaking waves can be described by an algebraic decay with depth is a striking result as it represents a large departure from the evanescent models used almost ubiquitously in models of surface gravity waves.

4.5. *Lagrangian drift at the surface*

We now focus on the drift velocity at the surface,

$$u_{L,s} = u_L(z_0 = 0). \tag{4.2}$$

Figure 8 shows the surface Lagrangian drift velocity $u_{L,s}$, scaled by c, the characteristic phase velocity of the packet. For non-breaking packets, the drift increases with S^2 as expected by linear and weakly nonlinear theory, and as already discussed before. We also show on figure 8 the data from Grue & Kolaas (2017) obtained for periodic trains of steep non-breaking waves in intermediate depth water (their wave frequency is 0.8 Hz, and water depth is 0.2 m). A sudden increase of the
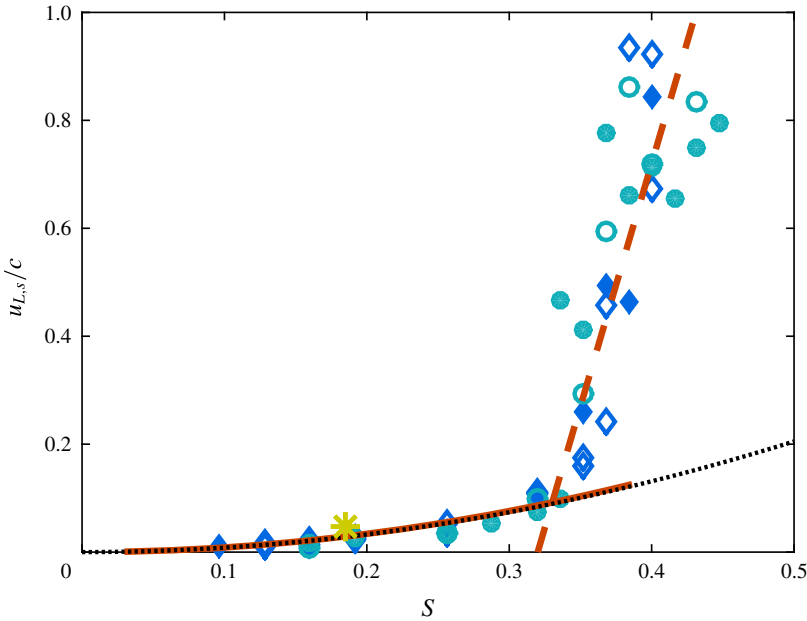
FIGURE 8. (Colour online) Surface drift velocity $u_{L,s}/c$, as a function of the wave slope S. $u_{L,s}$ increases with the slope. For non-breaking waves, $u_{L,s} \propto S^2$ and can be described by the linear theory (solid red line), equation (2.17), or by the simplified equation, $u_{L,s}/c = \chi_1 S^2$ (black dotted line), with $\chi_1 = 0.82$ a fitted parameter. The drift experiences a sharp increase for slopes above $S_* = 0.31$, which correspond to the appearance of breaking waves. For breaking waves we have $u_{L,s} \propto S$, as described by our scaling argument in § 2. The drift is then described, within the scatter of the data, by $u_{L,s}/c = \chi_2(S - S_*)$, with $\chi_2 = 9$ a fitted parameter. Circle and diamond symbols are numerical data for different runs, for two different mesh resolutions: open symbols are medium resolution and full symbols are high resolution, while diamonds are for $f_c = 0.87$ Hz, $\Delta f/f_c = 0.74$, and circles are for $f_c = 0.89$ Hz, $\Delta f/f_c = 0.75$. The yellow star is estimated from the experiments of Grue & Kolaas (2017) obtained in intermediate depth water.

Lagrangian drift is observed for breaking packets, where the drift increases linearly with the wave slope above threshold $S - S_*$.

The drift velocity at the surface for the non-breaking packets is well described by (2.17), with the amplitude of the wave component being evaluated using the initial shape of the wave packet, equation (3.2), as shown by the solid line on figure 8. Note that since our packet has a constant slope, the non-breaking packets can also be described by this simplified equation,

$$\frac{u_{L,s}}{c} = \chi_1 S^2, \quad \text{with } \chi_1 = 0.82, \tag{4.3}$$

which is the dotted line in figure 8, where $\chi_1 = 0.82$ is again obtained from the Stokes drift at the surface, equation (2.17), where the amplitude of each wave component was computed using the initial wave packet given by (3.2). This was already observed when rescaling the vertical profiles. These relations are valid for non-breaking packets, i.e. with slope $S < 0.31$ in the present configuration.

When the waves start to break ($S > 0.31$), the Lagrangian drift increases linearly with the slope above threshold $S - S_*$ and can be modelled by

$$\frac{u_{L,s}}{c} = \chi_2 (S - S_*), \quad \text{with} \quad \chi_2 = 9 \quad \text{and} \quad S_* = 0.31, \quad (4.4)$$

which is the dashed line in figure 8. The linear increase of the drift with S is suggested by the scaling argument presented in §2 and χ_2 is fitted to the data and is indeed $O(10)$ as expected by our scaling argument for the particle acceleration. S_* is an empirical breaking threshold determined for these focusing experiments.

5. Discussion and conclusion

We have presented numerical experiments and theory-based scaling of the Lagrangian drift, or mass transport, due to breaking waves in deep water. For non-breaking wave packets, the drift at the surface, as well as the exponential decay with depth is well described by the classical Stokes drift approach, generalized to a wave packet. A return flow is present at the bottom of the tank, consistent with mass conservation. We also observe that the drift is enhanced in the focusing region, as predicted by weakly nonlinear theory based on the nonlinear Schrödinger equation. In these non-breaking cases, the drift increases with the slope of the wave packet squared $u_L = \chi_1 c S^2$, where χ_1 is an $O(1)$ constant and c the central phase speed of the packet as predicted by linear theory. When the wave starts to break, an added drift due to breaking is observed at the surface, and is strongly localized around the break point. The depth profiles of the drift due to breaking are also changed and the initial depth of broken fluid scales with the height of the breaking waves. The decay with depth can be described by an exponential or algebraic law with this vertical scale. The added drift at the surface is up to an order of magnitude larger than the drift obtained for non-breaking packets. In these breaking cases, the drift increases linearly with the wave slope above threshold and can be described by $u_L = \chi_2 (S - S_*)$, where χ_2 is an order $O(10)$ constant and S_* is an empirical breaking threshold. The order of the constant χ_2, as well as the linear scaling with the slope can be explained by a scaling argument for particles being overtaken by the breaker, accelerated by gravity over a distance related to the breaking height.

These results shed light on the importance of breaking on the so-called Stokes drift, one of the keys to modelling the development of Langmuir circulations and upper ocean turbulence. As demonstrated by the laboratory measurements and scaling argument of Melville & Rapp (1988), even one very weak breaking wave per group was sufficient to double the average surface drift current above the classical Stokes drift. The even stronger contribution by breaking to the horizontal Lagrangian drift that we observe in these numerical experiments suggests that it could significantly affect these upper ocean processes, especially at submesoscales, and should be considered in further developments of coupled ocean–atmosphere models.

In the context of that modelling, it is clear that by combining experimental and numerical model results of single breaking events (Drazen *et al.* 2008; Romero *et al.* 2012; Deike *et al.* 2015, 2016; Pizzo *et al.* 2016) with field measurements of breaking statistics (Kleiss & Melville 2010; Sutherland & Melville 2013) following Phillips (1985), progress has been made in modelling the fluxes of momentum and energy from the wave field to the water column (Romero *et al.* 2012; Sutherland & Melville 2013, 2015) and bubble-mediated air entrainment (Deike *et al.* 2017). We are in the process of following the same approach in measuring and modelling the Lagrangian drift due to breaking and hope to report on those results in subsequent publications.

Appendix A. Validation and convergence of the results

We present in this appendix tests made to validate our numerical methods.

A.1. *Lagrangian transport*

The particle tracking method in the code Gerris has been detailed and validated in
previous studies of atomization processes (Tomar *et al.* 2010). Here we present a
test for the Lagrangian transport of a non-breaking Stokes wave. The simulation
is based on our earlier numerical configuration (see Deike *et al.* (2015) for detail).
The simulation domain is of one wavelength and is periodic in the propagation
direction, we work with a gravity wave of small slope $ak = 0.1$, where a is the
initial amplitude and $k = 2\pi/\lambda$ the wavenumber, λ the wavelength and $c_0 = \sqrt{g/k}$ the
phase velocity. Reynolds and Bond numbers are those used in Deike *et al.* (2015)
for gravity waves. The wave propagates in the x direction during a few wave periods
and is slowly damped by viscous dissipation. Lagrangian particles are placed in the
water domain, with initial position (x_0, z_0) and are tracked during the simulation. The
total Lagrangian drift is computed for each particle and then averaged horizontally
(phase averaged), leading to the drift velocity u_s. The horizontal drift velocity $u_s(z_0)$
is shown in figure 9 as a function of depth z_0/λ, and is very well described by
the theoretical Stokes drift for an irrotational monochromatic propagating wave of
amplitude a (described in §2, equation (2.10)), $u_s = c_0(ak)^2 e^{-2kz_0}$.

This non-breaking simple test validates the use of the particle tracking implemented
in Gerris and the ability of the code to study Lagrangian mass transport with sufficient
accuracy in the breaking case.

A.2. *Mass conservation*

The second important validation test regards mass conservation. We have shown in
earlier studies that mass is usually well conserved in Gerris including simulations of
complex breaking processes, including the formation of droplets and bubbles (Deike
et al. 2016). Figure 10 shows the error in mass conservation for two typical cases,
one non-breaking and one breaking. The error remains small, below 0.2 %, estimated
by normalizing the total volume measured in the simulation by the total volume
initially present. Note that the total volume is conserved by construction (air plus
water), however, some non-physical exchanges between the two phases can happen
during the interface reconstruction, when complex geometry, breaking, drops and
bubbles generation are solved, leading to an error in the mass conservation for each
phase (water or air), which we find is below 0.2 %. Note that the mass conservation
can also be estimated by estimating the variations in the mean water level, which is
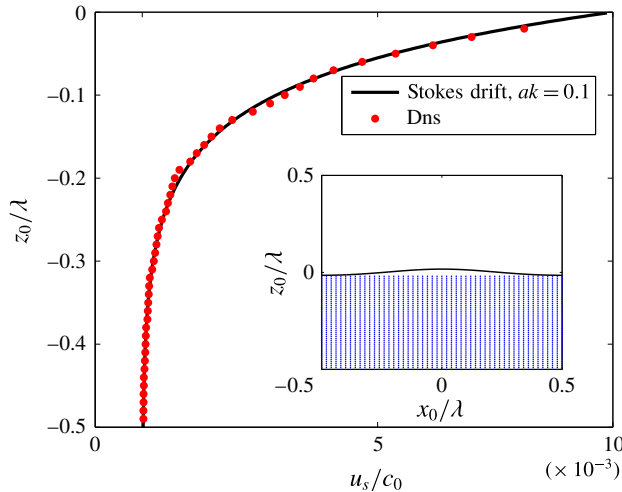found to be of the size of the mesh.

FIGURE 9. (Colour online) Lagrangian transport for a classic Stokes drift case with wave of slope $ak = 0.1$. Main figure: red symbols show the drift velocity u_s/c_0 as a function of the normalized initial vertical position z_0/λ. Here $u_s = \langle \Delta x \rangle / \mathcal{T}$, where $\langle \Delta x \rangle$ is the total particle displacement averaged horizontally and $\mathcal{T}$ the total time of the simulation, and c_0 is the wave phase velocity. The solid black line is the theoretical Stokes drift, $u_s = c(ak)^2 e^{2kz_0}$. Inset shows the initial location of the particles used to compute the Lagrangian drift.
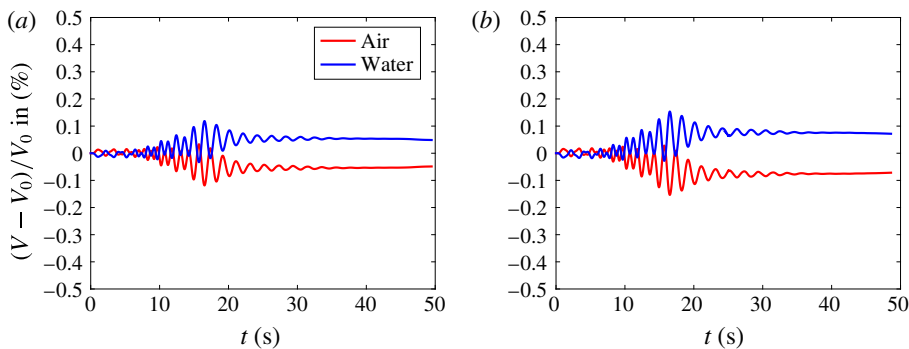

FIGURE 10. (Colour online) The error in conserving volume in each fluid, air and water, $(V_i - V_0)/V_0$, where V_0 is the initial volume (or mass) and V_i, the mass of air $(i = a)$ or water $(i = w)$. Two cases are shown, one non-breaking (a) $S = 0.3$ and one breaking (b) $S = 0.38$ packet. In both cases the maximum error is below 0.2%. Exchanges of volume between the two fluids are visible, showing total volume conservation while some error below 0.2% is observed on the mass conservation of each fluid.

Appendix B. Lagrangian transport in weakly nonlinear narrow-banded wave packets

To further elucidate the effects of nonlinearity on the Lagrangian transport, we now consider the nonlinear Schrödinger equation. Consider waves where the lowest mode has the form $Ae^{i\theta}$ where $A = A(X, T)$ and $\theta_x = k_0 + k$, $\theta_t = -\omega_0 - \omega$, $X = \epsilon x$, $T = \epsilon t$, where $\epsilon = a_0 k_0$ is a small parameter. This system has been studied extensively and

the governing equation, to $O(\epsilon^3)$, is the nonlinear Schrödinger equation, which may be written as

$$\mathrm{i}A_t + \mathrm{i}\frac{\omega_0}{2k_0}A_x - \frac{\omega_0}{8k_0^2}A_{xx} - \frac{\omega_0 k_0}{2}|A|^2 A = 0. \tag{B 1}$$

The velocity potential and free surface displacement for the waves are (Trulsen 2006; Pizzo 2015; Pizzo & Melville 2016)

$$\eta = \frac{1}{2}\left(\epsilon A \mathrm{e}^{\mathrm{i}\theta} + \epsilon^2 \frac{k_0}{2}A^2 \mathrm{e}^{2\mathrm{i}\theta} + \text{c.c.}\right), \tag{B 2}$$

$$\phi = \overline{\phi} + \frac{1}{2}\left(\left(-\epsilon\frac{\mathrm{i}\omega_0}{k_0}A + \frac{\epsilon^2 \omega_0}{k_0}\left(\frac{1}{2} - k_0 z\right)A_X\right)\mathrm{e}^{\mathrm{i}\theta}\mathrm{e}^{k_0 z} + \text{c.c.}\right), \tag{B 3}$$

where c.c. denotes complex conjugate.

The velocity, to second order in ϵ, then becomes

$$\frac{\mathrm{d}\xi}{\mathrm{d}t} = \phi_x|_{(x=\xi_0, z=\zeta_0)} = \frac{\omega_0}{2}\left(\left(\epsilon A - \frac{\mathrm{i}\epsilon^2}{k_0}\left(\frac{1}{2} + k_0\zeta_0\right)A_X\right)\mathrm{e}^{\mathrm{i}\theta_0}\mathrm{e}^{k_0\zeta_0} + \text{c.c.}\right) + O(\epsilon^3), \tag{B 4}$$

$$\frac{\mathrm{d}\zeta}{\mathrm{d}t} = \phi_z|_{(x=\xi_0, z=\zeta_0)} = \frac{\omega_0}{2}\left(\left(-\mathrm{i}\epsilon A - \frac{\epsilon^2}{k_0}\left(\frac{1}{2} + k_0\zeta_0\right)A_X\right)\mathrm{e}^{\mathrm{i}\theta_0}\mathrm{e}^{k_0\zeta_0} + \text{c.c.}\right) + O(\epsilon^3), \tag{B 5}$$

where $\theta_0 = k_0\xi_0 - \omega_0 t$.

By inspection, the solutions to these differential equations are

$$\xi - \xi_0 = \tfrac{1}{2}((\mathrm{i}\epsilon A + \epsilon^2\zeta_0 A_X)\mathrm{e}^{\mathrm{i}\theta_0}\mathrm{e}^{k_0\zeta_0} + \text{c.c.}) + O(\epsilon^3), \tag{B 6}$$

and

$$\zeta - \zeta_0 = \tfrac{1}{2}((\epsilon A - \mathrm{i}\epsilon^2\zeta_0 A_X)\mathrm{e}^{\mathrm{i}\theta_0}\mathrm{e}^{k_0\zeta_0} + \text{c.c.}) + O(\epsilon^3). \tag{B 7}$$

The Lagrangian velocity then may be found by expanding about the Eulerian velocity, and including the next terms in the Taylor expansion, so that the asymptotics are consistent for finding the third order Lagrangian drift for these waves. That is

$$\begin{aligned} U_L = {} & u(\xi_0, \zeta_0, t) + (\xi - \xi_0)\left(\frac{\partial u}{\partial x}\right)\bigg|_{(\xi_0,\zeta_0)} + (\zeta - \zeta_0)\left(\frac{\partial u}{\partial z}\right)\bigg|_{(\xi_0,\zeta_0)} \\ & + \frac{1}{2}\left((\xi - \xi_0)^2\left(\frac{\partial^2 u}{\partial x^2}\right)\bigg|_{(\xi_0,\zeta_0)} + (\zeta - \zeta_0)^2\left(\frac{\partial^2 u}{\partial z^2}\right)\bigg|_{(\xi_0,\zeta_0)} \right. \\ & \left. + 2(\zeta - \zeta_0)(\xi - \xi_0)\left(\frac{\partial^2 u}{\partial x \partial z}\right)\bigg|_{(\xi_0,\zeta_0)}\right) + O(\epsilon^4). \end{aligned} \tag{B 8}$$

Averaging over the phase then yields

$$u_L = \epsilon^2\frac{\omega_0}{k_0}k_0^2|A|^2\mathrm{e}^{2k_0\zeta_0} + \mathrm{i}\omega_0\epsilon^3\left(\frac{3}{4} + k_0\zeta_0\right)(AA_X^* - A^*A_X)\mathrm{e}^{2k\zeta_0} + \epsilon^3\,\overline{\phi}_x\big|_{z=0} + O(\epsilon^4), \tag{B 9}$$

where the mean Eulerian surface velocity $\overline{\phi}_x|_{z=0}$ is found by solving Laplace's equation subject to the boundary conditions $\overline{\phi}_z|_{z=0} = \omega_0/2|A|_X^2$ and that the mean flow vertical velocity goes to zero as $z \to -\infty$.

Now, the first term in (B 9) is the classical Stokes drift, as found in §2.1. The last term is due to the induced mean flow, due to gradients in the radiation stress of the wave packet. The second term is related to the mean wavenumber of the packet. To make this clearer, consider a compact wave packet, and integrate u_L over an interval so that the packet has completely passed a fixed location. Then,

$$\Delta x = \int u_L \, dt = \epsilon^2 c_0 k_0^2 E e^{2k_0 \zeta_0} + \epsilon^3 c_0 \left(\frac{3}{4} + k_0 \zeta_0 \right) P e^{2k \zeta_0}, \tag{B 10}$$

where $c_0 = \omega_0 / k_0$, E and P are two quantities that are conserved by the nonlinear Schrödinger equation, namely the action and the mean frequency. Specifically,

$$E = \int |A|^2 \, dt; \quad P = i \int (A A_X^* - A^* A_X) \, dt. \tag{B 11a,b}$$

As an example, consider a packet that takes the form $A = \text{sech}(x - \omega_0 / 2k_0 t) e^{iC_0 x^2 / 2}$ for C_0 a constant chirp. This implies shorter waves come before longer waves, leading to packet focusing, and $P > 0$. Note, the theory at this order still implies all particles experience the same drift.

REFERENCES

BANNER, M. L. & PEIRSON, W. L. 2007 Wave breaking onset and strength for two-dimensional deep-water wave groups. *J. Fluid Mech.* **585**, 93–115.

BELCHER, S. E., GRANT, A. L. M., HANLEY, K. E., FOX-KEMPER, B., VAN ROEKEL, L., SULLIVAN, P. P., LARGE, W. G., BROWN, A., HINES, A., CALVERT, D. *et al.* 2012 A global perspective on Langmuir turbulence in the ocean surface boundary layer. *Geophys. Res. Lett.* **39** (18).

VAN DEN BREMER, T. S. & TAYLOR, P. H. 2016 Lagrangian transport for two-dimensional deep-water surface gravity wave groups. *Proc. R. Soc. Lond.* A **472** (2192).

BRUCKER, K. A., O'SHEA, T. T., DOMMERMUTH, D. G. & ADAMS, P. 2010 Three-dimensional simulations of deep-water breaking waves. In *28th Symposium on Naval Hydrodynamics Pasadena, CA, USA*.

CAVALERI, L., FOX-KEMPER, B. & HEMER, M. 2012 Wind waves in the coupled climate system. *Bull. Am. Meteorol. Soc.* **93** (11), 1651–1661.

CHEN, G., KHARIF, C., ZALESKI, S. & LI, J. 1999 Two dimensionnal Navier–Stokes simulation of breaking waves. *Phys. Fluids* **11**, 121–133.

CLAMOND, D. 2007 On the Lagrangian description of steady surface gravity waves. *J. Fluid Mech.* **589**, 433–454.

CLEMENT, A. 1995 Coupling of two absorbing boundary conditions for 2d time-domain simulations of free surface gravity waves. *J. Comput. Phys.* **126**, 139–151.

CRAIK, A. D. D. & LEIBOVICH, S. 1976 A rational model for Langmuir circulations. *J. Fluid Mech.* **73** (03), 401–426.

DARWIN, C. 1953 Note on hydrodynamics. *Math. Proc. Camb. Phil. Soc.* **49** (02), 342–354.

D'ASARO, E. A. 2014 Turbulence in the upper-ocean mixed layer. *Annu. Rev. Mar. Sci.* **6**, 101–115.

DEIKE, L., LENAIN, L. & MELVILLE, W. K. 2017 Air entrainment by breaking waves. *Geophys. Res. Lett.* **44** (8), 3779–3787.

DEIKE, L., MELVILLE, W. K. & POPINET, S. 2016 Air entrainment and bubble statistics in breaking waves. *J. Fluid Mech.* **801**, 91–129.

DEIKE, L., POPINET, S. & MELVILLE, W. K. 2015 Capillary effects on wave breaking. *J. Fluid Mech.* **769**, 541–569.

DERAKHTI, M. & KIRBY, J. T. 2014 Bubble entrainment and liquid–bubble interaction under unsteady breaking waves. *J. Fluid Mech.* **761**, 464–506.

DERAKHTI, M. & KIRBY, J. T. 2016 Breaking-onset, energy and momentum flux in unsteady focused wave packets. *J. Fluid Mech.* **790**, 553–581.

DOMMERMUTH, D. G., YUE, D. K. P., LIN, W. M., RAPP, R. J., CHAN, E. S. & MELVILLE, W. K. 1988 Deep-water plunging breakers: a comparison between potential theory and experiments. *J. Fluid Mech.* **189**, 423–442.

DRAZEN, D. A. & MELVILLE, W. K. 2009 Turbulence and mixing in unsteady breaking surface waves. *J. Fluid Mech.* **628**, 85–119.

DRAZEN, D. A., MELVILLE, W. K. & LENAIN, L. 2008 Inertial scaling of dissipation in unsteady breaking waves. *J. Fluid Mech.* **611**, 307–332.

DUNCAN, J. H. 1981 An experimental investigation of breaking waves produced by a towed hydrofoil. *Proc. R. Soc. Lond.* A **377** (1770), 331–348.

DUNCAN, J. H., QIAO, H. & PHILOMIN, V. 1999 Gentle spilling breakers: crest profile evolution. *J. Fluid Mech.* **379**, 191–222.

EAMES, I., BELCHER, S. E. & HUNT, J. C. R. 1994 Drift, partial drift and darwin's proposition. *J. Fluid Mech.* **275**, 201–223.

FUSTER, D., AGBAGLAH, G., JOSSERAND, C., POPINET, S. & ZALESKI, S. 2009 Numerical simulation of droplets, bubbles and waves: state of the art. *Fluid Dyn. Res.* **41**, 065001.

FUSTER, D., MATAS, J.-P., MARTY, S., POPINET, S., HOEPFFNER, J., CARTELLIER, A. & ZALESKI, S. 2013 Instability regimes in the primary breakup region of planar coflowing sheets. *J. Fluid Mech.* **736**, 150–176.

GRARE, L., PEIRSON, W. L., BRANGER, H., WALKER, J. W., GIOVANANGELI, J.-P. & MAKIN, V. 2013 Growth and dissipation of wind-forced, deep-water waves. *J. Fluid Mech.* **722**, 5–50.

GRUE, J. & KOLAAS, J. 2017 Experimental particle paths and drift velocity in steep waves at finite water depth. *J. Fluid Mech.* **810**.

GRUE, J., KOLAAS, J. & JENSEN, A. 2014 Velocity fields in breaking-limited waves on finite depth. *Eur. J. Mech.* (*B/Fluids*) **47**, 97–107; enok Palm Memorial Volume.

HANEY, S., FOX-KEMPER, B., JULIEN, K. & WEBB, A. 2015 Symmetric and geostrophic instabilities in the wave-forced ocean mixed layer. *J. Phys. Oceanogr.* **45** (12), 3033–3056.

IAFRATI, A. 2011 Energy dissipation mechanisms in wave breaking processes: spilling and highly aerated plunging breaking events. *J. Geophys. Res.* **116** (C7).

JOHN, F. 1953 Two-dimensional potential flows with a free boundary. *Fritz John Collected Papers* **2**, 487.

KENYON, K. E. 1969 Stokes drift for random gravity waves. *J. Geophys. Res.* **74** (28), 6991–6994.

KLEISS, J. M. & MELVILLE, W. K. 2010 Observations of wave breaking kinematics in fetch-limited seas. *J. Phys. Oceanogr.* **40** (12), 2575–2604.

LIU, X. & DUNCAN, J. H. 2003 The effects of surfactants on spilling breaking waves. *Nature* **421**, 520–523.

LOEWEN, M. R. & MELVILLE, W. K. 1991 Microwave backscatter and acoustic radiation from breaking waves. *J. Fluid Mech.* **224**, 601–623.

LONGUET-HIGGINS, M. S. 1953 Mass transport in water waves. *Phil. Trans. R. Soc. Lond.* A **245** (903), 535–581.

LONGUET-HIGGINS, M. S. 1974 Breaking waves in deep or shallow water. In *Proc. 10th Conf. on Naval Hydrodynamics*, vol. 597.

LONGUET-HIGGINS, M. S. & STEWART, R. W. 1964 Radiation stresses in water waves; a physical discussion, with applications. In *Deep Sea Research and Oceanographic Abstracts*, vol. 11, pp. 529–562. Elsevier.

MCINTYRE, M. E. 1981 On the wave momentum myth. *J. Fluid Mech.* **106**, 331–347.

MCWILLIAMS, J. C. 2016 Submesoscale currents in the ocean. *Proc. R. Soc. Lond.* A **472** (2189).

MCWILLIAMS, J. C. & RESTREPO, J. M. 1999 The wave-driven ocean circulation. *J. Phys. Oceanogr.* **29** (10), 2523–2540.

MELVILLE, W. K. 1994 Energy dissipation by breaking waves. *J. Phys. Oceanogr.* **24** (10), 2041–2049.

MELVILLE, W. K. & RAPP, R. J. 1988 The surface velocity field in steep and breaking waves. *J. Fluid Mech.* **189**, 1–22.

MELVILLE, W. K. 1996 The role of surface wave breaking in air–sea interaction. *Annu. Rev. Fluid Mech.* **28**, 279–321.

MELVILLE, W. K. & RAPP, D. J. 1985 Momentum flux in breaking waves. *Nature* **317**, 514–516.

MONISMITH, S. G., COWEN, E. A., NEPF, H. M., MAGNAUDET, J. & THAIS, L. 2007 Laboratory observations of mean flows under surface gravity waves. *J. Fluid Mech.* **573**, 131–147.

PERLIN, M., CHOI, W. & TIAN, Z. 2013 Breaking waves in deep and intermediate waters. *Annu. Rev. Fluid Mech.* **45**, 115–145.

PHILLIPS, O. M. 1977 *The Dynamics of the Upper Ocean*. Cambridge University Press.

PHILLIPS, O. M. 1985 Spectral and statistical properties of the equilibrium range in wind-generated gravity waves. *J. Fluid Mech.* **156** (1), 505–531.

PIZZO, N. E. 2015, Properties of nonlinear and breaking deep-water surface waves. PhD thesis, University of California, San Diego.

PIZZO, N., DEIKE, L. & MELVILLE, W. K. 2016 Current generation by deep-water breaking waves. *J. Fluid Mech.* **803**, 275–291.

PIZZO, N. E. & MELVILLE, W. K. 2013 Vortex generation by deep-water breaking waves. *J. Fluid Mech.* **734**, 198–218.

PIZZO, N. E. & MELVILLE, W. K. 2016 Wave modulation: the geometry, kinematics, and dynamics of surface-wave packets. *J. Fluid Mech.* **803**, 292–312.

PIZZO, N. E. 2017 Surfing surface gravity waves. *J. Fluid Mech.* **823**, 316–328.

POPINET, S. 2003 Gerris: a tree-based adaptive solver for the incompressible Euler equations in complex geometries. *J. Comput. Phys.* **190**, 572–600.

POPINET, S. 2009 An accurate adaptive solver for surface-tension-driven interfacial flows. *J. Comput. Phys.* **228**, 5838–5866.

RAPP, R. J. & MELVILLE, W. K. 1990 Laboratory measurements of deep-water breaking waves. *Phil. Trans. R. Soc. Lond.* A **331**, 735–800.

ROMERO, L., MELVILLE, W. K. & KLEISS, J. M. 2012 Spectral energy dissipation due to surface wave breaking. *J. Phys. Oceanogr.* **42**, 1421–1441.

SCLAVOUNOS, P. D. 2005 Nonlinear particle kinematics of ocean waves. *J. Fluid Mech.* **540**, 133–142.

STOKES, G. G. 1847 On the theory of oscillatory waves. *Trans. Camb. Phil. Soc.* **8**, 441–473.

SULLIVAN, P. P. & MCWILLIAMS, J. C. 2010 Dynamics of winds and currents coupled to surface waves. *Annu. Rev. Fluid Mech.* **42**.

SUTHERLAND, P. & MELVILLE, W. K. 2013 Field measurements and scaling of ocean surface wave-breaking statistics. *Geophys. Res. Lett.* **40** (12), 3074–3079.

SUTHERLAND, P. & MELVILLE, W. K. 2015 Field measurements of surface and near-surface turbulence in the presence of breaking waves. *J. Phys. Oceanogr.* (45), 943–966.

TIAN, Z., PERLIN, M. & CHOI, W. 2010 Energy dissipation in two-dimensional unsteady plunging breakers and an eddy viscosity model. *J. Fluid Mech.* **655**, 217–257.

TIAN, Z., PERLIN, M. & CHOI, W. 2012 An eddy viscosity model for two-dimensional breaking waves and its validation with laboratory experiments. *Phys. Fluids* **24** (3), 036601.

TOMAR, G., FUSTER, D., ZALESKI, S. & POPINET, S. 2010 Multiscale simulations of primary atomization. *Comput. Fluids* **39** (10), 1864–1874.

TRULSEN, K. 2006 Weakly nonlinear and stochastic properties of ocean wave fields. Application to an extreme wave event. In *Waves in Geophysical Fluidssunamis, Rogue Waves, Internal Waves and Internal Tides*, pp. 49–106.

VINJE, T. & BREVIG, P. 1981 Numerical simulation of breaking waves. *Adv. Water Resour.* **4** (2), 77–82.